Applied Catalysis B: Environmental 188 (2016) 65–76

Contents lists available at ScienceDirect

Applied Catalysis B: Environmental

journal homepage: www.elsevier.com/locate/apcatb

Correlating the properties of hydrogenated titania to reaction kinetics and mechanism for the photocatalytic degradation of bisphenol A under solar irradiation

Evangelia Ioannidou[a], Alexandra Ioannidi[a], Zacharias Frontistis[a], Maria Antonopoulou[b], Charalampos Tselios[a], Dimitris Tsikritzis[a], Ioannis Konstantinou[b], Stella Kennou[a], Dimitris I. Kondarides[a], Dionissios Mantzavinos[a,*]

[a] Department of Chemical Engineering, University of Patras, Caratheodory 1, University Campus, GR-26504 Patras, Greece
[b] Department of Environmental & Natural Resources Management, University of Patras, 2 Seferi St., GR-30100 Agrinio, Greece

ARTICLE INFO

Article history:
Received 18 November 2015
Received in revised form 19 January 2016
Accepted 25 January 2016
Available online 28 January 2016

Keywords:
Activity
Annealing temperature
Catalyst characterization
Pathways
Sodium

ABSTRACT

Hydrogenation of a commercially available TiO_2 anatase catalyst was carried out at several annealing temperatures in the range 400–800 °C to improve its photocatalytic activity for the degradation of endocrine disruptor bisphenol A (BPA) under simulated solar irradiation. The prepared hydrogenated catalysts, as well as their counterparts calcined in air were characterized with respect to their morphological, optical and electronic properties by means of BET, XRD, XPS, DRS and UPS analyses. Thermal treatment under flowing hydrogen resulted in increased absorption at wavelengths below 400 nm, as well as in the appearance of a broad and almost uniform absorption band in the visible region, the intensity of which increased with increase of annealing temperature. The latter was attributed to the creation of gap states in the hydrogenated samples, which was not observed for the samples calcined in air. Interestingly, sodium inherently present in the bulk of the pristine catalyst was found to diffuse at the surface and this was more pronounced for the hydrogenated samples prepared at temperatures above 700 °C.

The relative catalytic activity was tested to degrade 240 μg/L BPA in pure water and it was found that the hydrogenated catalysts were more active than those calcined in air at the same temperatures. The maximum rate (0.0647 min^{-1}) was observed for the catalyst hydrogenated at 600 °C, i.e. three times greater than the respective calcined catalyst. Higher annealing temperatures had a detrimental effect on photocatalytic activity and this may be associated with a collapse of the specific surface area. Other than the annealing temperature, the rate was also strongly dependent on the water matrix (slower for more complex matrices), BPA and catalyst concentration and the presence of electron acceptors.

LC–MS/TOF analysis was employed to identify transformation by-products (TBPs) and elucidate reaction pathways. BPA degradation by hydrogenated catalysts seems to occur mainly through consecutive hydroxylation/oxidation reactions, as evidenced by the various oxygenated TBPs formed; conversely, scission of BPA through the isopropylidene group and further oxidation, yielding different para-substituted phenolic intermediates seems to be the main degradation route in the presence of calcined catalysts.

1. Introduction

Titanium dioxide has attracted significant interest in recent years due to its potential use in a variety of photo-induced processes, including photocatalytic production of hydrogen, decomposition of pollutants in air and water, and production of electricity with solar cells [1–3]. However, the efficiency of TiO_2 for solar-driven applications is limited, because, owing to its relatively large band gap energy (3.0–3.3 eV) [1], it can only absorb UV photons, which account for less than 5% of the total solar radiation that reaches the earth's surface. Therefore, much effort has been made to extend the working spectrum of TiO_2 toward the visible spectral region. This can be achieved by modifying the valence band of the semiconductor via non-metal ion doping [4] or by forming new donor states below the conduction band of TiO_2 with incorporation of metal ions into its crystal matrix [5]. An alternative method for improving the optical and photocatalytic properties of TiO_2 has been demonstrated recently by Chen et al. [6], who prepared disordered nanophase TiO_2 through hydrogenation of TiO_2 nanocrystals at 20 bar H_2 for 5 days. The so formed hydrogenated

* Corresponding author.
E-mail address: mantzavinos@chemeng.upatras.gr (D. Mantzavinos).

http://dx.doi.org/10.1016/j.apcatb.2016.01.060
0926-3373/

"black" TiO_2 was found to exhibit excellent activity and stability for the photocatalytic production of hydrogen from water. Since then, black TiO_2 and hydrogenated TiO_2-based photocatalysts have been synthesized by several different methods and studied for their photocatalytic performance for various environmental and energy-related applications [7–10]. In all cases, the hydrogenated TiO_2 (H-TiO_2) photocatalysts were characterized by enhanced visible-light absorption, which has been attributed to surface disorder and formation of Ti^{3+} defect sites and/or oxygen vacancies [6,7].

Interestingly, the use of hydrogenated titania for the photocatalytic degradation of pollutants has received mere attention in recent studies by Teng et al. [9] and Saputera et al. [10]. Both articles focused on the synthesis and characterization of hydrogenated titania samples followed by photocatalytic activity testing for the decolorization of rhodamine [9] and methyl orange [10] in water. The occurrence and advanced treatment of persistent micro-pollutants in various aqueous matrices has received great attention in the past 10–15 years and several classes of compounds have been classified as priority pollutants [11]. Amongst others, endocrine disrupting compounds (EDCs) have consistently been detected in various matrices including drinking water [12]. Bisphenols, and in particular BPA, are xenoestrogens belonging to the EDCs family and they are suspected of adverse human health effects [13].

In the present work, several TiO_2 photocatalysts were prepared by heat-treatment in the range 400–800 °C either under flowing hydrogen or in air and they were fully characterized regarding their physicochemical, optical and electronic properties. The catalysts were then screened to evaluate their relative catalytic activity for BPA degradation under simulated solar irradiation, while the most effective sample was tested further to investigate the effect of various operating conditions on kinetics, reaction mechanisms and pathways. In this frame, we propose a systematic approach comprising two crucial elements, namely (i) the preparation and detailed characterization of relatively new photocatalytic materials with enhanced properties, and (ii) thorough testing of such materials for environmental applications, i.e. treatment of waters contaminated by emerging micro-pollutants. Unlike most previous studies in the field that concentrate on either element, this work gives new insights how catalyst properties can influence its environmental performance.

2. Materials and methods

2.1. Preparation of photocatalysts

The hydrogenated titanium dioxide photocatalysts were prepared by heat-treatment of commercial Hombikat UV-100 powder (Sachtleben Chemie, 99.9%) under flowing hydrogen. For this, an amount of the parent TiO_2 powder was placed in a quartz tube and heated at the desired temperature (400, 500, 550, 600, 650, 700 or 800 °C) under flowing nitrogen with a heating rate of 15 °C/min. The flow was then switched to hydrogen (80 cm^3/min) and the sample was maintained at that temperature for a period of 5 h. Finally, the powder was cooled down to room temperature under N_2 flow and stored in sealed vials for further use. The H_2-treated photocatalysts are denoted as H-TiO_2(T), where T indicates the reduction temperature. For comparison purposes, the same procedure was followed to prepare TiO_2 samples calcined in air at the same temperatures, denoted as TiO_2(T). A list of the synthesized H-TiO_2(T) and TiO_2(T) samples is shown in Table 1.

2.2. Chemicals and matrices

Bisphenol A ($C_{15}H_{16}O_2$, CAS number 80-05-7) and Degussa P25 TiO_2 (CAS number 13463-67-7) were purchased from Sigma-Aldrich and used as received. Most of the experiments were carried out in ultrapure water (UPW, pH 6) taken from a water purification system (EASYpureRF-Barnstead/Thermolyne, USA). Commercially available bottled water (pH 7.5, 0.4 mS/cm conductivity containing 211 mg/L bicarbonate, 10 mg/L chloride, 15 mg/L sulfate, 5 mg/L nitrate and 78 mg/L of various metal ions) was employed for experiments in drinking water (DW) matrix. Humic acid (HA, CAS number 1415-93-6) added in UPW was purchased from Sigma-Aldrich. Secondary treated wastewater (WW) was taken from the university campus treatment plant (pH 8, COD = 21 mg/L). *tert*-Butanol (CAS number 75-65-0) used as radical scavenger was purchased from Sigma-Aldrich. pH adjustment to acidic and alkaline conditions was done adding sulfuric acid and sodium hydroxide, respectively.

2.3. Experimental procedure

Slurry photocatalytic experiments were conducted in an open-to-air, glass, cylindrical vessel containing 120 mL of the reaction mixture. The vessel was irradiated from the top using a solar simulator (Oriel, model LCS-100, equipped with a 100 W xenon ozone-free lamp) and its contents were magnetically stirred at ambient conditions. The incident radiation intensity in the UV region of the electromagnetic spectrum was measured using ferrioxalate as the chemical actinometer and it was found to be 7.3×10^{-7} einstein/(L.s). For those runs performed under visible light, a filter with a 420 nm cut-off was employed (Newport FSQ-GG420, 50.8 mm × 50.8 mm). Prior to irradiation, the suspension was left 15 min in the dark to equilibrate. Most photocatalytic experiments were performed in duplicate and mean values, whose standard deviation never exceeded 5%, are quoted as results.

2.4. Characterization of photocatalysts

The physicochemical and optical properties of the synthesized samples were investigated employing nitrogen physisorption at the temperature of liquid nitrogen (BET method), X-ray diffraction (XRD), and UV–vis diffuse reflectance spectroscopy (DRS). Results obtained were used to estimate the specific surface area (SSA), phase composition and primary crystallite size of TiO_2, and optical band gap of the semiconductors, respectively. The experimental methods and procedures employed have been described in detail elsewhere [14,15].

X-ray photoelectron spectroscopy (XPS) measurements were obtained with the use of an unmonochromatized Mg Kα line at 1253.6 eV (12 keV with 20 mA anode current) and an analyzer (Leybold EA-11) with a pass energy of 100 eV and a resolution of 1.3 eV, estimated from the full width at half maximum (FWHM) of Au 4f 7/2 peak. XPS analysis was carried out at 0° take-off angle (normal to the sample surface). In all XP spectra, the binding energy (BE) of the adventitious carbon 1s peak at 285 eV was used as a measured BE reference. Ultra Violet Photoelectron spectroscopy (UPS) measurements were taken using a He I (21.2 eV) excitation line. A bias voltage of 12.23 V was applied to the specimen in order to separate the high binding energy cut-off from the analyzer.

2.5. Measurement of BPA concentration

High performance liquid chromatography (Waters Alliance 2695) was employed to monitor the concentration of BPA according to the protocol described elsewhere [16].

2.6. Measurement of total organic carbon

Total organic carbon (TOC) in the liquid phase was measured with an Aurora 1030W analyzer.

Table 1
Characteristics of the H-TiO_2(T) and TiO_2(T) photocatalysts.

Sample notation	Calcination temperature (°C)/gas atmosphere	SSA[a] (m^2/g)	TiO_2 phase composition (wt.% anatase)	Primary crystallite size[b] (nm)	E_{bg}[c] (eV)
TiO_2 (UV-100)	–	197	100	9	3.19
TiO_2(400)	400/air	105	100	14	3.17
TiO_2(500)	500/air	77	100	16	3.17
TiO_2(550)	550/air	55	100	18	3.16
TiO_2(600)	600/air	45	100	20	3.16
TiO_2(650)	650/air	36	100	23	3.16
TiO_2(700)	700/air	22	100	28	3.16
TiO_2(800)	800/air	11	100	38	3.15
H-TiO_2(400)	400/H_2	107	100	12	3.14
H-TiO_2(500)	500/H_2	101	100	14	3.15
H-TiO_2(550)	550/H_2	66	100	17	3.13
H-TiO_2(600)	600/H_2	40	100	22	3.12
H-TiO_2(650)	650/H_2	18	100	28	3.11
H-TiO_2(700)	700/H_2	14	96	29	3.08
H-TiO_2(800)	800/H_2	2	33	47	2.46

[a] Specific surface area determined with the BET method.
[b] Primary size of anatase TiO_2 crystallites estimated from XRD line broadening.
[c] Band gap energy, estimated from Tauc plot.

2.7. Analysis of transformation by-products (TBPs)

An LC–MS/TOF instrument (UPLC Dionex Ultimate 3000 by Thermo coupled with a Focus microTOF II—time of flight mass spectrometer by Brüker Daltonics, Germany) in negative and positive ionization mode was used for the identification of TBPs generated during BPA photocatalysis. Pre-concentrated samples were analysed on a C18 Acclaim™ RSLC, 100 mm × 2.1 mm i.d., 2.2 μm particle size (Thermo Fisher Scientific, San Jose, USA). For the analysis, the SPE method and the chromatographic conditions reported in our earlier study [16] were applied.

2.8. Toxicity

The luminescent marine bacteria *Vibrio fischeri* were used to assess the acute ecotoxicity of BPA prior to and after photocatalytic treatment according to the procedures described elsewhere [16].

3. Results and discussion

3.1. Characteristics of TiO_2(T) and H-TiO_2(T) photocatalysts

3.1.1. Specific surface area, phase composition and crystallite size

The XRD patterns of the TiO_2(T) and H-TiO_2(T) samples are shown in Fig. 1a and b, respectively. For comparison purposes, the diffractogram of the pristine TiO_2 powder (Hombikat UV-100) is shown in both graphs. The average crystallite size of the materials was estimated from the major diffraction peak of anatase TiO_2 ($2\theta = 25.17°$), according to the Scherrer equation, and results obtained are summarized in Table 1. In the same table are listed the specific surface areas (SSA) of all samples, measured with the BET method. For comparison purposes, results of BET and XRD experiments are shown graphically in Fig. 2, where the SSA (Fig. 2a) and mean crystallite size (Fig. 2b) of the TiO_2(T) and H-TiO_2(T) samples are plotted as function of the annealing temperature.

The parent material (UV-100) is a semi-crystalline mesoporous TiO_2 powder [10] which consists only of the anatase phase and possesses high surface area of *ca.* 200 m^2/g (Table 1). Calcination of this sample in air for 5 h at temperatures up to 800 °C results in a progressive decrease of SSA from 197 to 11 m^2/g (Table 1). This is accompanied by a drastic improvement of the crystallinity of TiO_2, which is evidenced by the narrower and sharper XRD reflections (Fig. 1a) and the formation of larger crystallites (Fig. 2b). Interestingly, the anatase phase of TiO_2 is retained for all TiO_2(T) samples and is the only phase detected even after calcination in air at 800 °C (Fig. 1a). This observation is in agreement with results of previous studies where Hombikat UV-100 was used as the starting material [10,17,18]. It is known that the anatase phase of TiO_2 is normally converted to the rutile phase at temperatures above 600 °C [2]. with the exact transformation temperature depending on several factors, including the degree of crystallinity and crystallite size of TiO_2 [19–21] and the presence of dopants in the bulk or on the surface [22,23]. The stability of the anatase phase observed for the present TiO_2(T) samples may be associated to the amorphous nature of the starting material and the presence of impurities, such as Na (see Section 3.1.3), in the crystal matrix of UV-100.

Qualitatively similar results were obtained for the H-TiO_2(T) samples prepared in hydrogen atmosphere, with the exception that conversion of anatase to rutile starts to take place at *ca.* 700 °C (Fig. 1b) and becomes significant for the sample treated in H_2 flow at 800 °C, where the mass fraction of anatase decreases to 33% (Table 1). This indicates that the hydrogenation promotes phase transformation of anatase to rutile TiO_2, which can be explained by considering that the point defects created in the TiO_2 crystal structure under reducing atmosphere favor and accelerate the lattice rearrangement that leads to conversion of anatase to rutile [24]. Regarding the SSA of the H-TiO_2(T) samples, it is relatively high for samples prepared at 400–500 °C. However, an increase of temperature above 650 °C has a detrimental effect on SSA, which drops to 2 m^2/g for the H-TiO_2(800) sample (Fig. 2a, Table 1). This is accompanied by the progressive growth of the grain size of the samples (Fig. 2b), caused by the high surface energy of the nanocrystalline particles, which leads to a densification of the material.

3.1.2. Optical properties

The UV–vis DR spectra of selected TiO_2(T) and H-TiO_2(T) samples are shown Fig. 3a and b, respectively. The band gap energy (E_{bg}) of each semiconductor was estimated according to the Tauc method, as described elsewhere [14], and results obtained are summarized in Table 1. The parent UV-100 TiO_2 absorbs at wavelengths shorter than *ca.* 400 nm and has an optical band gap of 3.19 eV. Heat treatment in air results in a small red shift of the absorption spectra of all TiO_2(T) samples (Fig. 3a), which is reflected to their slightly lower E_{bg} (3.15–3.17 eV) (Table 1). This is accompanied by a significant increase of absorption in the UVA region, which can be attributed to the higher crystallinity and larger crystallite size of the heat-treated samples.

Regarding the H-TiO_2(T) samples, it is observed that treatment in H_2 atmosphere in the temperature range of 400–700 °C results in increased absorption at wavelengths shorter than 400 nm and in

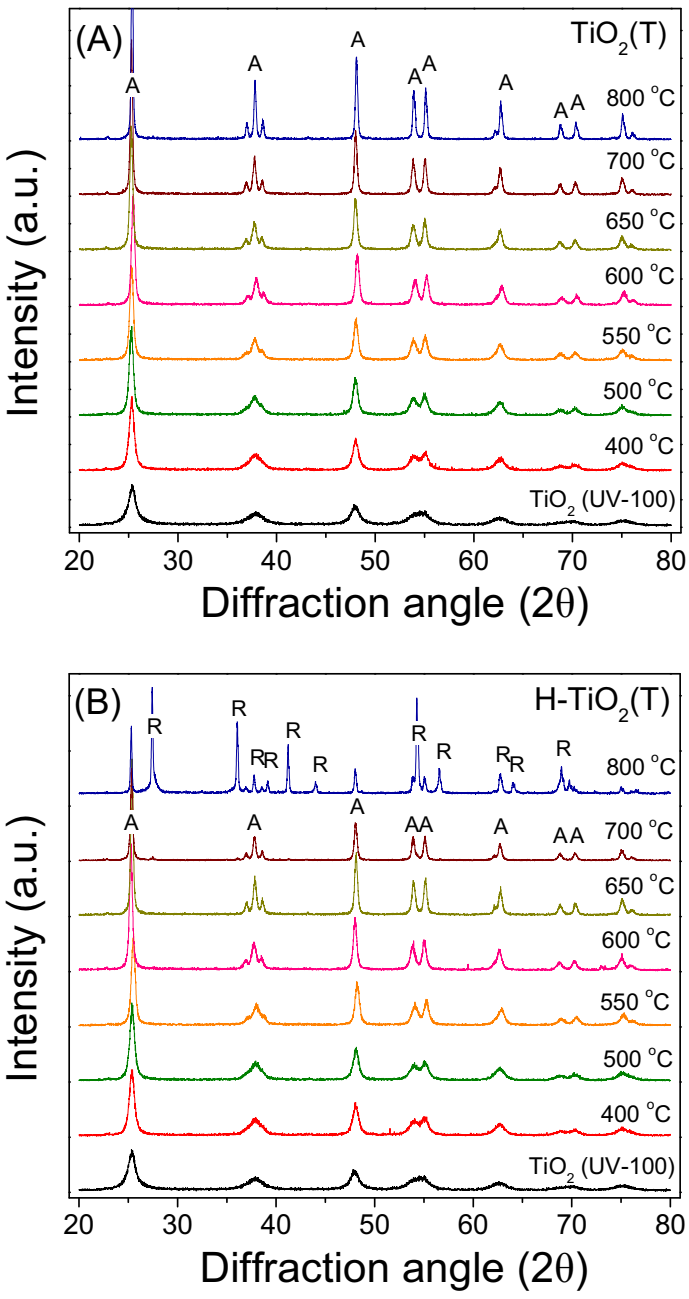

Fig. 1. X-ray diffraction patterns of (a) TiO_2(T) and (b) H-TiO_2(T) catalysts prepared by heat treatment of Hombikat UV-100 TiO_2 powder at the indicated temperatures under air or H_2 flow, respectively. The XRD pattern of the parent TiO_2 sample is also shown for comparison. Diffraction peaks denoted as "A" and "R" refer to the anatase and rutile TiO_2 phases, respectively.

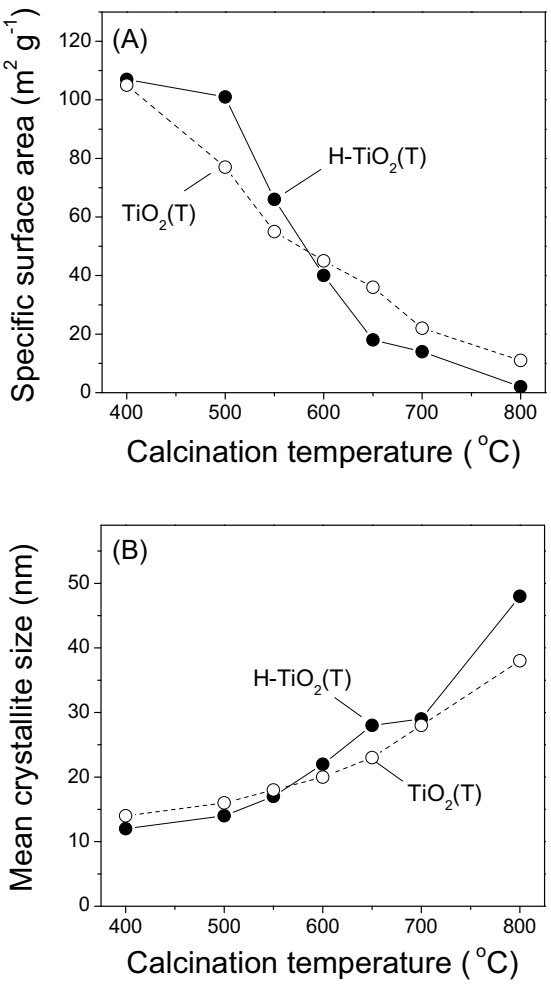

Fig. 2. Effects of annealing temperature on (a) the specific surface area and (b) the mean primary crystallite size of anatase TiO_2 for the studied TiO_2(T) and H-TiO_2(T) samples.

a progressive shift of the absorption edge toward the visible region (Fig. 3b). The corresponding decrease of E_{bg} is small, but generally higher than that observed for TiO_2(T) samples calcined in air at the same temperatures (Table 1). The effects of hydrogenation on the optical properties become much more pronounced upon further increase of annealing temperature at 800 °C, which results in a significant red shift of the absorption edge (E_{bg} = 2.46 eV). An important characteristic of the DR spectra of the H-TiO_2(T) samples is the appearance of a broad and almost uniform absorption band in the visible region, the intensity of which increases with an increase of the annealing temperature (Fig. 3b). The visible absorption of the H-TiO_2(T) samples is evident by visual inspection. In particular, the initially white UV-100 TiO_2 powder turns to pale yellow (T = 400 °C), yellowish grey (T = 500–550 °C), light grey (T = 600–700 °C) and, eventually, dark grey (T = 800 °C), upon increasing temperature under flowing H_2. In contrast, the TiO_2(T) powders calcined in air at the same temperatures are all white in color. The improved absorption of the H-TiO_2(T) samples at wavelengths longer than *ca.* 400 nm is in agreement with results of previous studies [6,10,25–27] and can be attributed to the excitation of conduction band electrons associated to oxygen vacancies formed by hydrogenation. The degree of hydrogenation of TiO_2 achieved upon thermal treatment under hydrogen atmosphere and, therefore, the optical characteristics of the final material depend on several factors, including the pressure and concentration of H_2 gas, the reaction time and temperature as well as the phase composition and morphological characteristics of the starting TiO_2 material [28,29].

3.1.3. Surface chemical composition

XPS measurements were obtained for TiO_2(T) and H-TiO_2(T) samples treated at temperatures of 500, 600, 700 or 800 °C. In Fig. 4a are shown typical Ti2p spectra obtained for selected samples. It is observed that the Ti2p3/2 peak appears at a binding energy of 458.5 eV with a splitting from the Ti2p1/2 peak equal to 5.7 eV, which corresponds to TiO_2 [30]. Similar results were obtained for all samples investigated, indicating that, under the present experimental conditions, Ti is not affected by heat treatment in air or H_2 atmosphere since no Ti^{3+} peak was detected. In Fig. 4b are shown

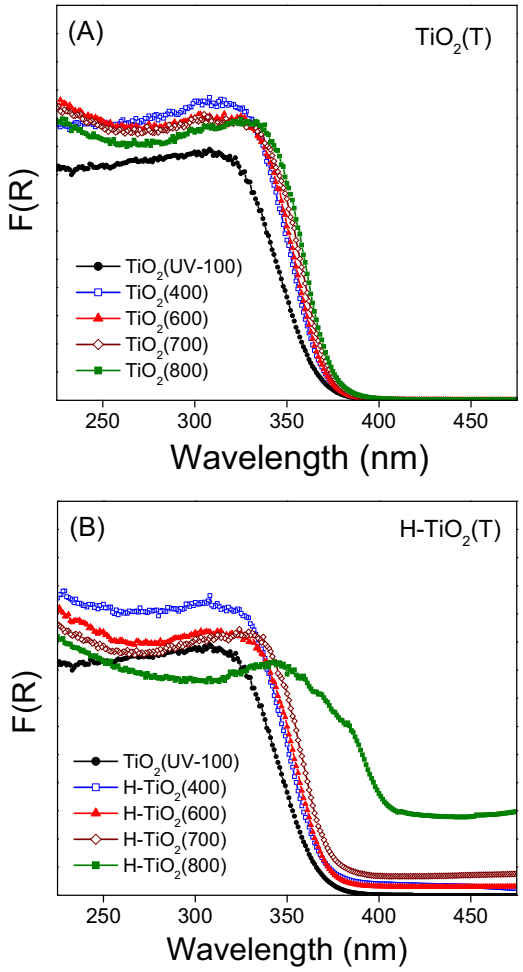

Fig. 3. Representative UV–vis diffuse reflectance spectra obtained for (a) TiO_2(T) and (b) H-TiO_2(T) samples treated at the indicated temperatures. The DR spectrum of the parent TiO_2 material is also shown, for comparison.

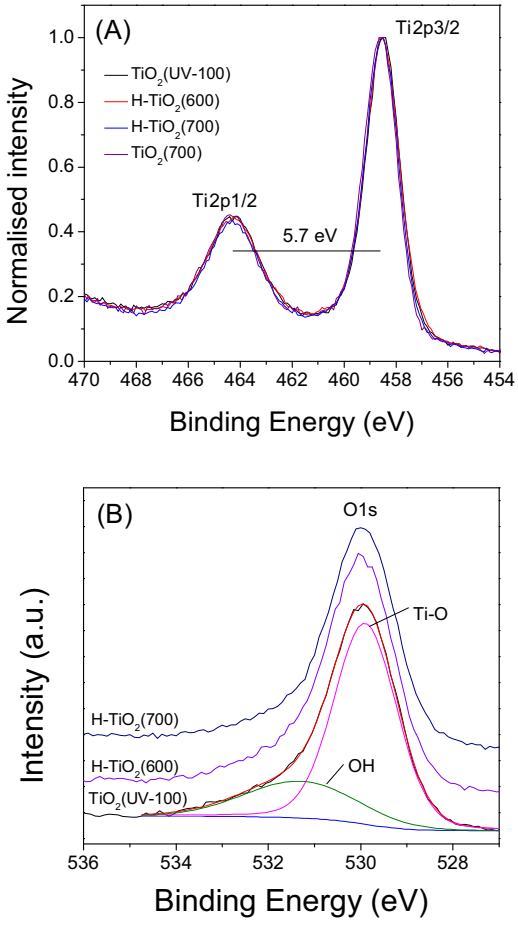

Fig. 4. (a) XPS spectra in the Ti2p region obtained for the indicated samples; (b) O1s XPS spectra of UV-100 TiO_2, H-TiO_2(600) and H-TiO_2(700) samples.

Table 2
Atomic ratios of O/Ti and Na/Ti for selected H-TiO_2(T) and TiO_2(T) photocatalysts.

Sample	O/Ti ratio	Na/Ti ratio
TiO_2 (UV-100)	2.2	–
TiO_2(500)	2.1	–
TiO_2(600)	2.6	–
TiO_2(700)	2.5	0.03
TiO_2(800)	2.5	0.10
H-TiO_2(500)	2.4	–
H-TiO_2(600)	2.4	0.06
H-TiO_2(700)	2.3	0.10
H-TiO_2(800)	2.7	0.60

representative O1s XPS spectra of UV-100 TiO_2, H-TiO_2(600) and H-TiO_2(700), which are similar to those obtained for all TiO_2(T) and H-TiO_2(T) samples investigated. In all cases, the O1s peak was fitted to a main peak at a binding energy of 529.9 eV, which corresponds to the oxide, and a shoulder at a binding energy of 531.3 eV which corresponds to OH-groups (Fig. 4b). Although the OH peak for the H-TiO_2(T) samples is slightly greater than the TiO_2(T) samples, safe conclusions cannot be derived since the presence of OH-groups is, most likely, due to the exposure of the samples to the atmosphere.

A very interesting finding of the XPS measurements is the appearance of a peak located at a binding energy of 1071.5 eV, which corresponds to Na1s. This peak, which is not observed in the XP spectrum of the parent UV-100 TiO_2, becomes clearly observable for the H-TiO_2(600) sample and increases significantly in intensity with increase of annealing temperature in hydrogen atmosphere (Fig. 5a). Qualitatively similar results were obtained for the TiO_2(T) samples (not shown for brevity). The atomic ratios O/Ti and Na/Ti were estimated from the XPS spectra and results are summarized in Table 2. For comparison purposes, the atomic ratio Na/Ti is plotted in Fig. 5b as a function of annealing temperature for all H-TiO_2(T) and TiO_2(T) samples investigated. It is clearly observed that increase of treatment temperature results in an increase of the amount of Na at the surface of TiO_2, which is much more pronounced for H-TiO_2(T) compared to TiO_2(T) samples.

In order to exclude the possibility of contamination of the samples by Na during preparation (furnace, reactor walls, etc.), a second H-TiO_2(800) specimen was prepared in a different apparatus, which gave exactly the same results. In addition, when another type of commercial TiO_2 powder (Degussa P25) was treated in H_2 atmosphere at the same temperature (800 °C), only trace amounts of Na were detected by XPS (Na/Ti atomic ratio of 0.05). Thus, it is concluded that the Na detected on the surface of the heat-treated samples originates from the material itself. According to the supplier, commercial Hombikat UV-100 powder contains traces of sodium, which are not detectable by XPS for the as received sample. Evidently, increase of annealing temperature results in diffusion of Na atoms from the bulk to the surface of TiO_2, a process which is strongly favored under H_2 atmosphere (Fig. 5b). Similar results have been reported by Feng et al. [31], who investigated the effects of heating in air on the surface Na content of a (not specified) TiO_2 powder. The authors observed increasing photoemission of Na-related orbitals with increasing temperature of the

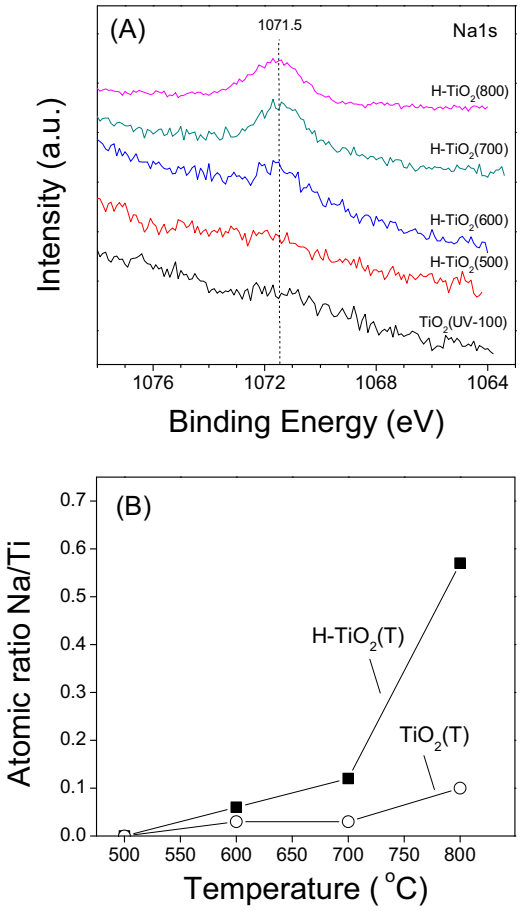

Fig. 5. (a) Na1s XPS spectra of H-TiO_2(T) samples prepared by hydrogenation at the indicated temperatures; (b) Effect of annealing temperature on the Na/Ti atomic ratio measured for the studied TiO_2(T) and H-TiO_2(T) samples.

sample and identified the TiO_2 powder itself as the source of the temperature-enriched Na on the surface of TiO_2 crystallites [31]. A similar enrichment of the TiO_2 surface by Na upon hydrogenation has been reported by Teng et al. [9], who prepared black TiO_2 using a process that involved pretreatment of the starting material (Degussa P25 powder) with a NaOH solution. Generally, the mobility of Na ions in TiO_2 increases with temperature increment [32,33].

3.1.4. Electronic structure

The valence band (VB) spectra obtained for the parent UV-100 TiO_2 and the hydrogenated H-TiO_2(T) samples annealed at 500, 600, 700 and 800 °C are shown in Fig. 6 (left part). The region near the Fermi level is shown in more detail in the right part of the same figure. It is observed that the untreated sample exhibits a broad peak between 6 and 8 eV. Heat treatment results in improved crystallinity of TiO_2 (see Section 3.1.1). As a result, the spectra of the hydrogenated samples are characterized by the presence of two clearly distinguishable peaks located at *ca.* 6 and 8 eV, which can be attributed to the Ti 3d-O2p π-bonding state and Ti 3d-O 2p σ-bonding state [34].

The valence band maximum (VBM) of UV-100 TiO_2 is located at 2.9 ± 0.2 eV below the Fermi level (Fig. 6, right part). This shows that the Fermi level of the as-received sample is close to the conduction band of the semiconductor, which confirms the n-type character of the TiO_2 sample. Hydrogenation at temperatures in the range 500–700 °C results in additional electronic states above the valence band maximum, at 2.1 ± 0.2 eV for H-TiO_2(500), 2.0 ± 0.2 eV for H-TiO_2(600) and 1.6 ± 0.2 eV for H-TiO_2(700) from the Fermi level. This behavior is in agreement with results reported in a previous study [35], where hydrogenation of TiO_2 was achieved at a constant temperature and different pressures. Interestingly, the VB spectrum of the H-TiO_2(800) sample is similar to that of the untreated UV-100 TiO_2 (Fig. 6), most probably due to hydrogen desorption during high temperature treatment.

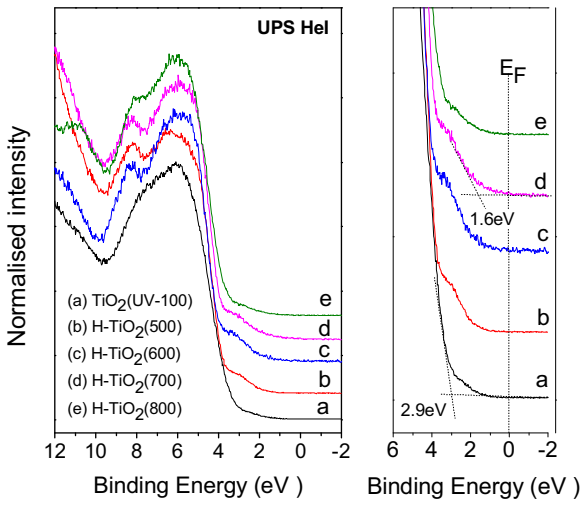

Fig. 6. UPS spectra obtained for the untreated TiO_2 (UV-100) and the H-TiO_2(T) samples prepared by hydrogenation at the indicated temperatures. The region near the Fermi level is expanded in the right part of the Figure.

Results presented in Fig. 6 provide evidence that treatment of TiO_2 with hydrogen at high temperatures results in the creation of gap states and, concomitantly, in a decrease of the effective band gap of the semiconductor. In contrast, the VB spectra of the TiO_2(T) samples calcined in air (not shown for brevity) do not show any gap states, thereby confirming that the shift of the VBM (Fig. 6) originates from the hydrogenation of TiO_2. These additional electronic states inside the band gap of TiO_2 are related to the wide wavelength absorption of H-TiO_2(T) samples in the visible region (Fig. 3b) in agreement with previous observations and calculations [36].

3.2. Assessment of relative catalytic activity

To evaluate the relative catalytic activity of the H-TiO_2(T) and TiO_2(T) samples, experiments were conducted at 240 μg/L BPA concentration, 100 mg/L catalyst concentration, and inherent solution pH (~6), under either solar or visible radiation. Fig. 7a shows representative concentration-time profiles for certain catalysts under solar radiation, where the H-TiO_2(600) sample exhibits the highest activity with complete BPA conversion in 30–45 min; the time needed to achieve complete conversion with the TiO_2(600) sample is longer than 120 min. Concentration profiles can be fitted to a first order kinetic expression with respect to BPA concentration and the computed apparent rate constants, k_{app}, are given in Fig. 7b. It is observed that the H-TiO_2(T) catalysts are generally more active than their TiO_2(T) counterparts; k_{app} increases progressively with an increase in calcination temperature, goes through a maximum at T = 600 °C and then decreases at higher temperatures. This trend also occurs, to a lesser extent though, for the TiO_2(T) samples. The rate constant for the H-TiO_2(600) sample is 0.0647 min^{-1}, which is three times greater than the value for the TiO_2(600) sample or the pristine Hombikat UV-100 (i.e. last bar of Fig. 7b).

The results from the respective experiments in the visible (>420 nm) are shown in Fig. 7c, where the relative catalytic performance is qualitatively similar to that under solar radiation.

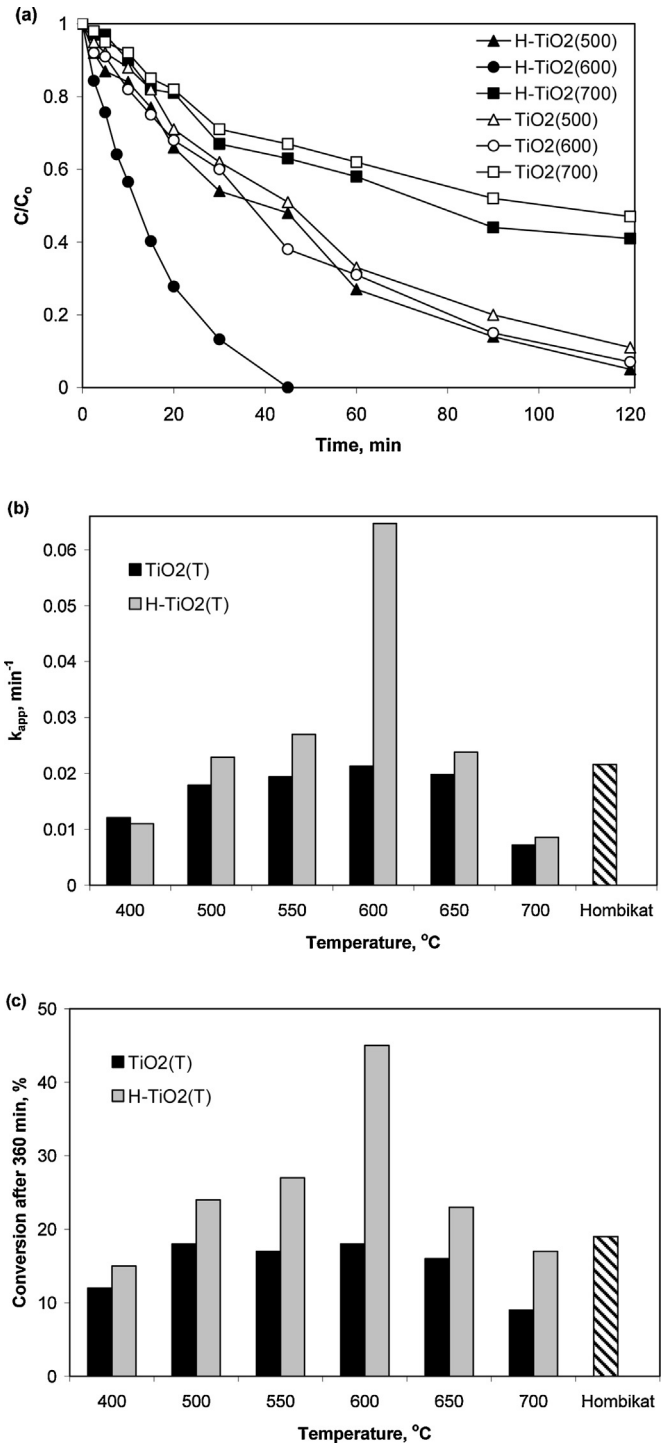

Fig. 7. Comparison of catalytic activity of H-TiO_2(T) and TiO_2(T) catalysts (100 mg/L) for the degradation of 240 μg/L BPA in UPW and inherent pH. (a) Concentration-time profiles under solar radiation; (b) apparent rate constants under solar radiation; (c) 360-min conversion under visible radiation.

However, reaction rates in the visible are substantially lower, which shows the dominant role of the UVA fraction of the simulated solar light on BPA photocatalytic degradation. For instance, the H-TiO_2(600) sample results in 45% conversion after 360 min in the visible but this conversion can be achieved after only 10 min under solar radiation (Fig. 1a). This is consistent with other studies reporting that H-TiO_2 photocatalysts do not fully exploit visible light for the photocatalytic processes and the enhanced efficiency of these materials is associated mainly with the UV region [6,7].

Results presented in Fig. 7b shows a volcano-type effect of annealing temperature on the apparent reaction rate for both the TiO_2(T) and H-TiO_2(T) catalysts. Regarding the TiO_2(T) samples, the observed variation of k_{app} on calcination temperature should not be attributed to differences in the phase composition of TiO_2 because, according the XRD results, all TiO_2(T) samples consist of anatase TiO_2 (Table 1, Fig. 1a). Thus, the increase of k_{app} with increase of calcination temperature from 400 to 600 °C could be attributed to the progressive increase of the crystallite size and the enhanced crystallinity of TiO_2 (Fig. 2b), which is known to result in suppression of the electron-hole recombination rate and to facilitate interfacial charge transfer processes [37]. On the other hand, heat treatment also results in a decrease of the specific surface area, which becomes significant for samples calcined above 600 °C (Fig. 2a). Concomitantly, this leads to a decrease of the amount of surface sites available for adsorption and/or dark reactions. Thus, the observation of a maximum for the TiO_2(600) sample may be attributed to the counter-acting effects of crystallite size and specific surface area on photocatalytic performance. Qualitatively similar results, showing a maximum of photocatalytic activity for TiO_2 samples treated at different temperatures, have been reported in the literature [18].

The improved activity of H-TiO_2(T), compared to TiO_2(T) samples, can be attributed to the hydrogenation, i.e., incorporation of hydrogen into the TiO_2 lattice, which is evidenced by the formation of band gap states in the electronic structure of TiO_2 (Fig. 6). Similar results have been published recently by Chen et al. [36], who reported that the gap states caused from the hydrogenated disordered surface layer are responsible for the visible and infrared absorption of black titania nanoparticles. It has been reported [8,38] that oxygen vacancies may suppress the recombination of photogenerated electrons and holes, thereby improving the photocatalytic activity. (Nonetheless, the role of vacancies in relation to the recombination rate is controversial, as will be discussed in Section 3.3) Qualitatively similar results have been reported by Amano and Nakata [39], who investigated the effects of hydrogen reduction on the photocatalytic performance of rutile TiO_2 for water oxidation and found that the optimum hydrogenation temperature of rutile TiO_2 for water oxidation was 700 °C, and by Saputera et al. [10] who found that the highest photocatalytic activity of hydrogenated TiO_2 P25 was obtained for samples treated at 500 °C.

Regarding the potential role of Na diffused on the photocatalyst surface upon annealing at high temperatures (Fig. 5), a detailed investigation of this issue is beyond the scope of the present work. It has been reported that modification of TiO_2 by small quantities of Na may enhance activity, e.g., for the photocatalytic reduction of CO_2 [40]. However, results of preliminary experiments performed with the use of TiO_2 (UV-100) promoted with small amounts of Na (0.05, 0.1 and 0.2 wt.%) showed that addition of Na results in a decrease of activity for the title reaction (results not shown for brevity). This issue will be the subject of our future investigation.

According to these findings, all subsequent experiments were performed with H-TiO_2(600) catalyst under solar radiation.

3.3. Dependence of kinetics on the operating variables and matrices

Fig. 8 shows the effect of initial BPA concentration in the range 120–750 μg/L on degradation with complete conversion occurring in less than 90 min irrespective of the concentration. For the experiments performed at 120 and 240 μg/L, the reaction rate is, indeed, first order since the apparent rate constant is common (0.0637 ± 0.001 min^{-1}); as the concentration increases though, the rate constant decreases and this denotes a transition from first to lower order kinetics (although data fitting to a pseudo-first order expression is still adequate). At a simple level, the rate of reactive oxygen species (ROS) formation should solely be a function of pho-

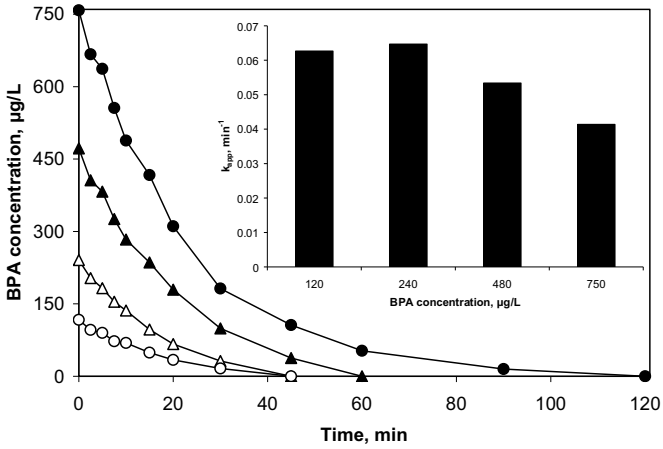

Fig. 8. Effect of BPA concentration on degradation at 100 mg/L H-TiO_2(600) in UPW and inherent pH. Inset graph shows apparent rate constants.

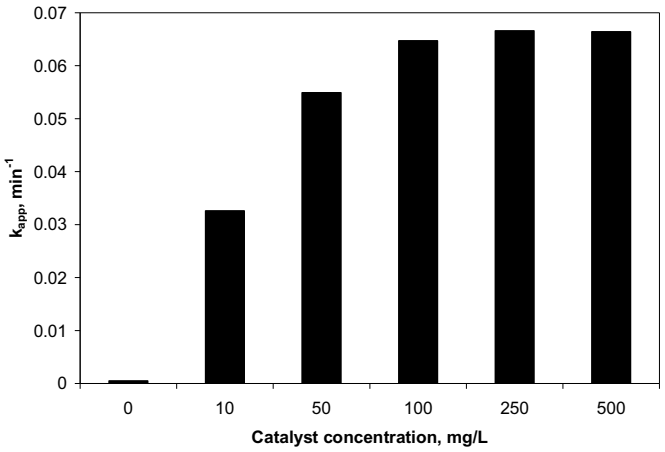

Fig. 9. Effect of H-TiO_2(600) concentration on 240 μg/L BPA degradation in UPW and inherent pH.

ton flux and the catalyst concentration [41] and, therefore, nearly constant for the experiments of Fig. 8. At increased BPA concentrations, ROS concentration becomes the limiting reactant and this explains a shift from first to lower (and eventually zeroth) order kinetics.

As clearly seen in Fig. 9, BPA degradation is exclusively due to the interaction between photons and the catalyst since photolysis alone does not contribute to the process. Typical to slurry systems, the rate increases with increasing catalyst concentration up to a point (between 50 and 100 mg/L in this work) beyond which it reaches a plateau; this corresponds to a concentration of active sites high enough to absorb all of the available photons [42].

The addition of electron acceptors, such as oxygen or H_2O_2, in the reaction mixture is a typical approach to enhance photocatalytic performance. Fig. 10 shows the beneficial impact of H_2O_2 addition up to 100 mg/L, which leads to a linear increase of the apparent rate constant. Hydrogen peroxide scavenges conduction band electrons, thus (i) generating more hydroxyl radicals, and (ii) reducing the extent of hole-electron recombination, both of which would contribute to increased degradation rates [15].

Environmentally relevant samples contain organic and inorganic constituents that usually interfere with ROS and, consequently, affect degradation kinetics. This is clearly demonstrated in Fig. 11a, which shows BPA degradation in various actual and synthetic matrices. The presence of various anions (bicarbonates, sulfates and chlorides) and metal ions in DW that may act as ROS

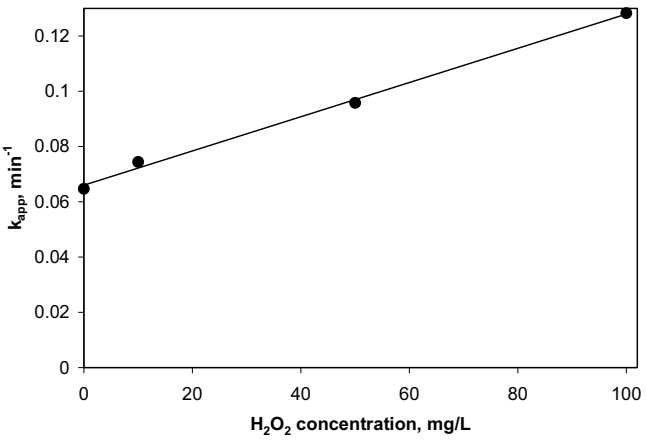

Fig. 10. Effect of H_2O_2 addition on 240 μg/L BPA degradation at 100 mg/L H-TiO_2(600) in UPW and inherent pH.

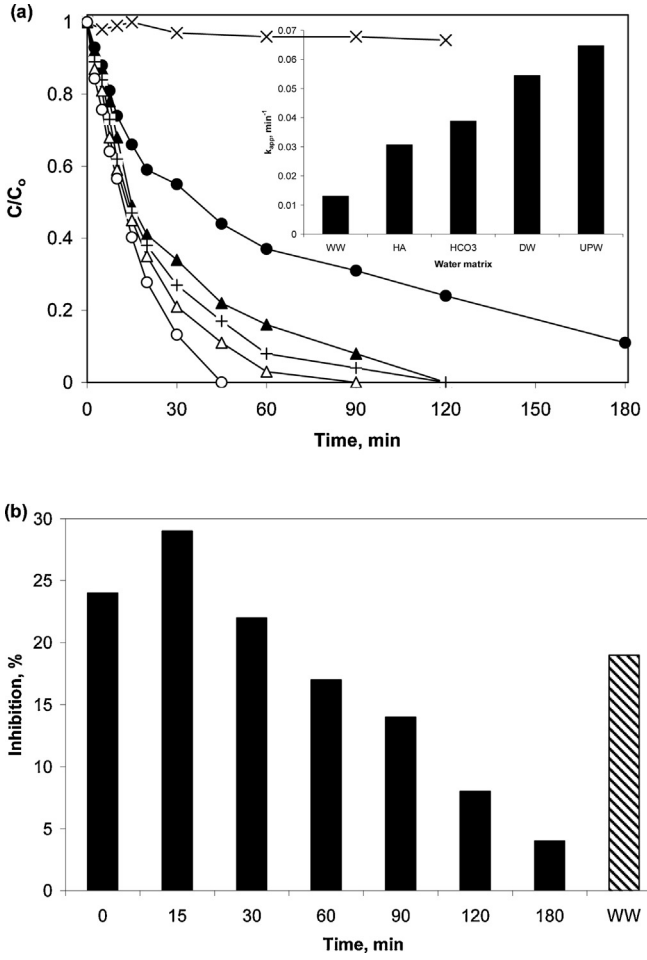

Fig. 11. Effect of water matrix on 240 μg/L BPA degradation at 100 mg/L H-TiO_2(600). (a) Concentration-time profiles and apparent rate constants (inset graph); (b) changes in toxicity in WW.
-O- UPW; -Δ- DW; -+- 500 mg/L HCO_3^- in UPW; -▲- 10 mg/L humic acid in UPW; -●- WW; -X- 250 mg/L *tert*-butanol in UPW.

scavengers [43] and/or block catalyst active sites [44] explains the reduced degradation (15% in terms of k_{app}) in comparison to UPW. The role of bicarbonates as hydroxyl radical scavengers to form carbonate radicals is well-documented [45] and this is demonstrated in the run where 500 mg/L of bicarbonates (this is about 2.5 times the concentration in DW) have been spiked in UPW; in this case,

the rate constant is 40% lower than that in UPW and is associated with the fact that carbonate radicals have lower oxidizing ability (about 25%) than hydroxyl radicals [46].

Besides the negative effect of inorganics on degradation, the organic content of environmental samples may also affect kinetics. The addition of 10 mg/L of humic acid in UPW to mimic the resistant natural organic matter of waters/wastewaters nearly halves the degradation rate; this is so since HA competes with BPA for the catalyst active sites and the photogenerated ROS, while it may also attenuate the incident light in the suspension [47]. This effect is more pronounced when *tert*-butanol, an effective radical scavenger, is added in UPW at a concentration which is three orders of magnitude greater than BPA; as seen in Fig. 11a, the reaction is completed quenched.

The combined detrimental effect of organics and inorganics on degradation is exemplified in the run with WW, where the rate is five times lower than in UPW. It should be noted here that for the various matrices tested in this work, their inherent pH differs by about two units, i.e. 6 in UPW and 8 in WW. To test whether pH is critical to BPA degradation, an additional experiment was performed in UPW under alkaline conditions; the rate constant was found to increase from 0.0647 to 0.09 min^{-1} although complete BPA conversion occurred after 45 min irrespective of the solution pH (data not shown for brevity).

For the run in WW, the inhibition to *V. fischeri* was followed throughout the course of the reaction; as seen in Fig. 11b, BPA at 240 μg/L is not toxic since inhibition is marginally greater than the inherent value of the WW sample, which is shown at the last bar. Interestingly, inhibition slightly increases during the early stages of the reaction but consistently decreases thereafter, which implies that photocatalytic treatment is capable of removing inhibitory compounds originally present in WW.

A final set of experiments was performed to assess catalyst reusability, as follows: 240 μg/L of BPA and 100 mg/L H-TiO_2(600) were loaded in the reaction vessel and treated for 45 min, i.e. the time needed to achieve complete BPA removal according to Fig. 7a; at the end of the experiment, the reaction mixture was fed an additional 240 μg/L of BPA, treated for another 45 min and this procedure was repeated four times. Fig. 12a shows concentration profiles for the five consecutive cycles, where one can see that the catalyst partially loses its activity since the 45-min conversion decreases from 100% to 74% between the first and the last cycle; in terms of apparent rate constants shown in Fig. 12b, the respective reduction is 45%. This may be ascribed to the progressive increase of the organic content of the solution due to the accumulation of TBPs and residual, unreacted BPA that are carried over from one cycle to the next. Moreover, some of these intermediates may strongly be adsorbed on the catalyst surface, thus reducing the number of active sites available for reaction. Saputera et al. [10] reported that the activity of hydrogenated titania to degrade methyl orange decreased 4-fold (in terms of rate constants) after three consecutive cycles. This loss of activity was lower (about 1.6 times) when titania was doped with platinum.

The stability of the hydrogenated TiO_2 catalysts seems to depend on the synthesis method employed, the anatase/rutile content of the final material and the reaction conditions used for photocatalytic tests. Although oxygen vacancy and Ti^{3+} sites located at the photocatalyst surface are expected to disappear quickly under oxidative reaction conditions, it is possible to synthesize hydrogenated TiO_2 samples with bulk defects [48] or to form specific, room-temperature-stable defect structures [28]. For instance, Liu et al. [28] reported that high pressure hydrogenation of commercial TiO_2 powders can create highly active anatase and anatase/rutile photocatalysts, which exhibit excellent long-term stability for H_2 evolution. However, this was not the case when rutile TiO_2 was used [28].

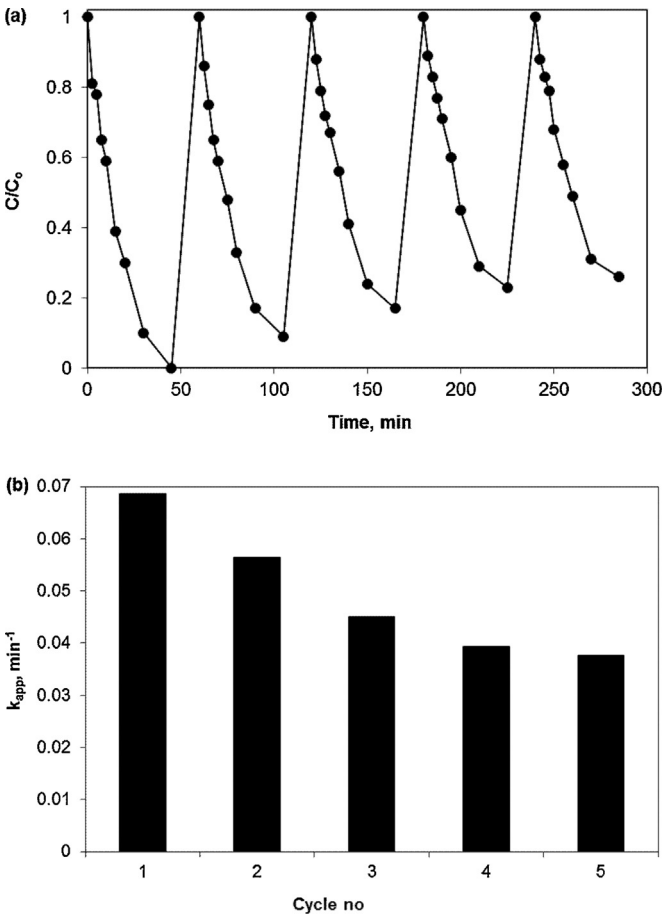

Fig. 12. Activity of H-TiO_2(600) (100 mg/L) in five consecutive cycles. (a) Concentration-time profiles; (b) apparent rate constants.

It is generally believed that the presence of lattice defects in semiconductor photocatalysts promotes electron-hole recombination and, therefore, results in lower reaction rates. In the case of TiO_2, the density of oxygen vacancy and Ti^{3+} defects can be decreased by calcination of the material in air at high temperatures [49]. which usually results in enhanced photocatalytic performance (e.g. Fig. 7). However, results of recent studies over rutile [39,50] and anatase [51] TiO_2 showed that the presence of only few oxygen vacancies in the lattice may have the opposite effect, i.e., to suppress photocatalytic activity, because of the decreased n-type conductivity of the semiconductor. In this respect, Amano et al. [39,50] provided evidence that oxygen vacancies and/or Ti^{3+} species are necessary elements for photocatalytic reactions to proceed, and concluded that the increased activity of hydrogen-treated TiO_2 may be related to the higher density of photogenerated charge carriers induced by the presence of these defects. Other authors simply proposed that oxygen defects present in hydrogenated TiO_2 samples improve photocatalytic performance by suppressing the recombination of photogenerated charge carriers [8,38,52,53].

In addition to the above possible roles of lattice defects, results of the present and previous studies of hydrogenated TiO_2 catalysts show that creation of oxygen vacancies results in increased response of the photocatalyst to the solar spectral region, thereby enhancing its visible light photoactivity. It should be noted, however, that the overall effect of high-temperature hydrogenation of TiO_2 on its photocatalytic performance is very complex because, as has been discussed in Section 3.1, it also influences other important physicochemical characteristics of the material, including crystallinity, primary crystallite size and specific surface area of TiO_2.

3.4. TBPs and reaction pathways

Analysis by LC–MS/TOF allowed the identification of eight and four TBPs during BPA photocatalytic degradation in the presence of H-TiO_2(600) and TiO_2(600), respectively. Data obtained from LC–MS/TOF analysis (calculated mass of negative/positive pseudo-molecular ions, MS fragments, mass errors and the proposed empirical formula for each TBP) are summarized in Tables 3 and 4. Accurate mass measurements (<5 ppm error) provided by the TOF analyzer provide strong evidence for the assignment of their molecular formula.

In the case of the photocatalytic degradation of BPA in the presence of H-TiO_2(600), mono- and poly-hydroxylated TBPs (243, 275B) were identified, in agreement with previous studies focused on the removal of BPA by various AOPs [16,54,55]. Furthermore, the activation of a hydroxylated aromatic ring towards electrophilic attack by other HO• radicals is well documented in the literature [16,56].

Three TBPs (225, 241, 257) were recognized as oxidized products with an aldehyde and/or keto structures. Based on literature data, oxidized products can be formed through direct oxidation of hydroxyl groups of their primary TBPs. Alternatively, addition of O_2 to a carbon-centred radicals after hydrogen abstraction by HO• attack can form TBPs with carbonyl functional group [56,57].

The TBP 275A was formed via the rupture of the aromatic ring and corresponds to an oxygenated ring opening product in the form of bi-carboxylic acid group. A TBP (325) with higher molecular weight than BPA, eluting at 9.2 min was also detected and can be formed by secondary reactions between oxidation products of BPA. The same structures have been proposed by Deborde et al. [54] during the oxidation of BPA by ozone in aqueous solution. TBP 149 is attributed to monohydroxylated-4-isopropenylphenol formed from the cleavage of the single bond between the isopropylidene carbon and the phenyl groups of BPA and further dealkylation and oxidation reactions. A comparison of the peak areas of the TBPs reveals that hydroxyl-TBPs are the most abundant intermediates followed by oxidized-TBPs, whereas the remaining/others are only present at trace quantities.

During the photocatalytic degradation of BPA using TiO_2(600) as photocatalyst, oxidation leads to different para-substituted phenols. TBPs labeled as 135A, 135B and 149 were attributed to 4-hydroxyacetophenone, 4-isopropenylphenol and monohydroxylated-4-isopropenylphenol respectively, generated by cleavage of the single bond between the isopropylidene carbon and the phenyl group of BPA, in agreement with previous studies [16,58,59]. The scission of the bond between the isopropylidene carbon and the phenyl group was also found to be the main pathway of $^1O_2$ induced phototransformation [59].

The degradation pathways revealed differences among the used catalysts (Figs. 13 and 14). The photocatalytic degradation mechanism in the presence of H-TiO_2(600) has been demonstrated to occur mainly through mono-hydroxylation of BPA followed by (a) oxidation of the hydroxyl group to give keto intermediates, (b) further hydroxylation to give di-hydroxy-TBPs, (c) ring opening. Another minor but later stage pathway involves reaction between the generated TBPs. Hydroxyl radicals are generated through the oxidation of OH^- and H_2O by holes photogenerated during the irradiation of H-TiO_2 with light energy greater than its band gap energy. Moreover, the creation of oxygen vacancies in the lattice associated with the presence of Ti^{3+} states as well as the reduction of electron-hole pair recombination rate due to the reaction between surface sites with O_2 in TiO_2 photocatalysts have been found to play an essential role in photocatalytic process over H-TiO_2 photocatalysts [6,10]. According to literature data, Ti^{3+} surface sites react easily with O_2, leading to the formation of reactive radicals such as $O_2^{\bullet-}$,$HO_2^{\bullet-}$, and HO• [60]. which are consistent with

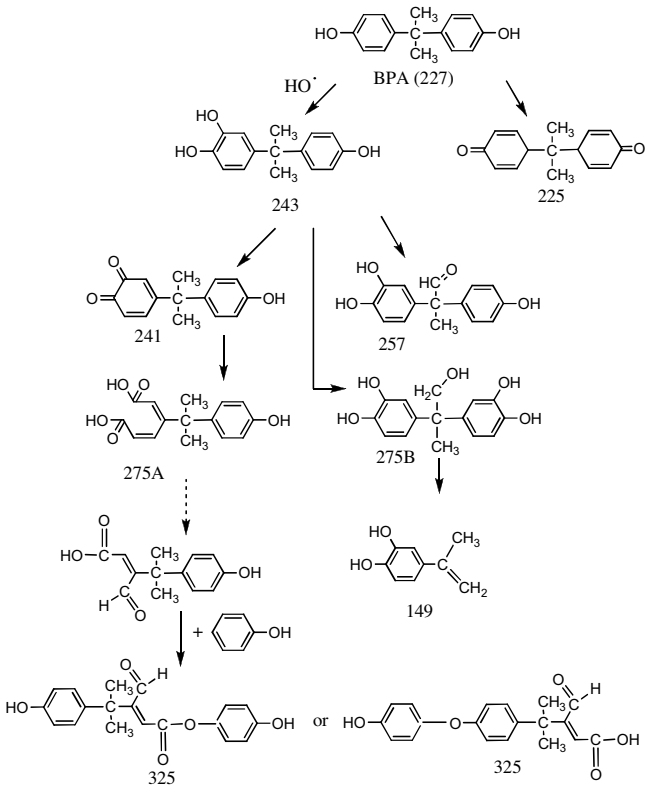

Fig. 13. Photocatalytic degradation pathways of BPA in the presence of H-TiO_2(600).

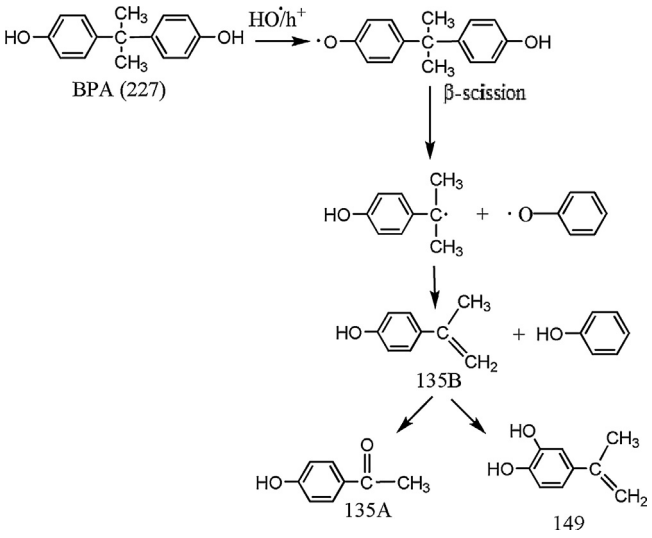

Fig. 14. Photocatalytic degradation pathways of BPA in the presence of TiO_2(600).

the detected TBPs. The fact that XPS does not show the formation of surface Ti^{3+} species at measurable amounts indicates that they are present only in a subsurface configuration or in a concentration below the detection limit of XPS.

On the other hand, degradation of BPA using TiO_2(600) occurs via cleavage of the molecule through the isopropylidene group and further oxidation, yielding different para-substituted phenolic intermediates. Interestingly, based on the non-detection of hydroxylated TBPs, hydroxylation degradation pathways were minor in this case. Initially, holes and/or HO• oxidize the phenol moiety of BPA by one electron transfer generating a phenoxyl radical as the first step. The phenoxylradical is stabilized by electron resonance within the phenol ring and undergoes β-scission (cleavage

Table 3
LC–MS-TOF high resolution accurate mass data ([M−H]⁻, MS fragment ions and relative error Δ(ppm)) for BPA and its TBPs during degradation with H-TiO_2(600).

R_t (min)	Pseudo-Molecular Formula	m/z [M−H]⁻	Δ (ppm)	MS fragments	Δ (ppm)
8.2	$C_{15}H_{15}O_2$	227.1072 (BPA)	2.4	211.1136$C_{15}H_{15}O$	−3.6
7.6	$C_{15}H_{15}O_3$	243.1024 (243)	1.1	229.0870$C_{14}H_{13}O_3$ 227.1068$C_{15}H_{15}O_2$	0.1 4.2
7.3	$C_{15}H_{13}O_3$	241.0867 (241)	1.3	226.0628$C_{14}H_{10}O_3$ 211.0760$C_{14}H_{11}O_2$	3.3 2.1
6.4	$C_{15}H_{13}O_4$	257.0820 (257)	0.3	245.0818$C_{14}H_{13}O_4$	0.5
6.2	$C_{15}H_{15}O_5$	275.0925 (275B)	−0.3	261.0756$C_{14}H_{13}O_5$ 259.0969$C_{15}H_{15}O_4$	0.6 −1.6
6.5	$C_{15}H_{15}O_5$	275.0913 (275A)	4.4	257.0829$C_{15}H_{13}O_4$	−3.8
6.6	$C_9H_9O_2$	149.0605 (149)	2	–	–
9.2	$C_{19}H_{17}O_5$	325.1081	0.1	–	–
10.5	$C_{15}H_{13}O_2$	225.0924	−1.30	–	–

Table 4
LC–MS-TOF high resolution accurate mass data ([M−H]⁻, [M+H]⁺, MS fragment ions and relative error Δ(ppm)) for BPA and its TBPs during degradation with TiO_2(600).

R_t (min)	Pseudo-Molecular Formula	m/z [M−H]⁻	Δ (ppm)	MS fragments	Δ (ppm)
8.2	$C_{15}H_{15}O_2$	227.1072 (BPA)	2.4	211.1136$C_{15}H_{15}O$	−3.6
6.4	$C_{15}H_{13}O_4$	257.0820 (257)	0.3	245.0818$C_{14}H_{13}O_4$	0.5
6.1	$C_8H_7O_2$	135.0451 (135A)	0.4	–	–
6.6	$C_9H_9O_2$	149.0605 (149)	2	–	–
R_t (min)	Pseudo-Molecular Formula	m/z [M+H]⁺	Δ (ppm)	MS fragments	Δ (ppm)
6.2	$C_9H_{11}O$	135.0804 (135B)	2.5	–	–

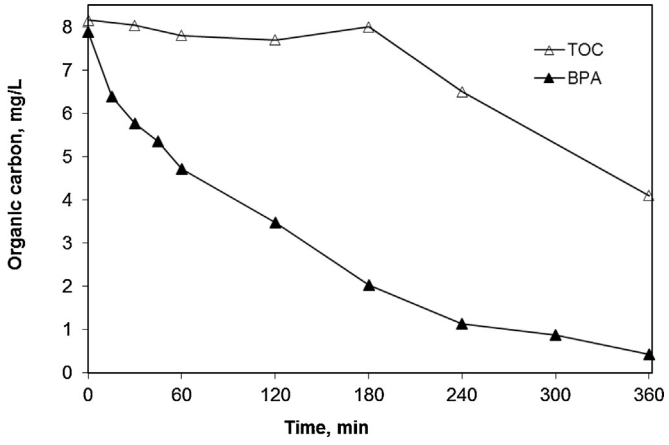

Fig. 15. Mineralization of 10 mg/L BPA at 1 g/L H-TiO_2(600).

between the benzene rings and the isopropyl group) to form 4-isopropenylphenol and phenol.

A final experiment was performed to assess the ability of the proposed system to mineralize BPA. To allow for an accurate determination of TOC in the liquid phase, the run was performed at an increased BPA concentration of 10 mg/L in the presence of 1 g/L H-TiO_2(600). Fig. 15 shows the TOC-time profile, as well as BPA profile in the form of its organic carbon content. Although BPA can nearly completely be removed (i.e. 95%) after 360 min of reaction, TOC decreases by only about 50%, which indicates that TBPs are more resistant than the parent compound to total oxidation to carbon dioxide and water. Notably, partial oxidation reactions (i.e. BPA conversion to TBPs and transformations amongst TBPs as shown in Fig. 13) exclusively occur during the first 180 min since TOC remains unchanged.

4. Conclusions

The main findings of this work are summarized as follows:

(1) Annealing of TiO_2 powder (Hombikat UV100) in air or hydrogen atmosphere at temperatures in the range of 400–800 °C results in a progressive increase of the primary crystallite size of TiO_2 and a concomitant decrease of the specific surface area. The hydrogenated H-TiO_2(T) samples are characterized by increased absorption in the UVA region and by a broad and almost uniform absorption band in the visible region, the intensity of which increases with an increase of annealing temperature. Interestingly, heat-treatment also results in enrichment of the photocatalyst surface with Na, originating from diffusion of impurities present in the bulk of the material, which is strongly favored under H_2 atmosphere.
(2) The photocatalytic activity of both TiO_2(T) and H-TiO_2(T) samples for the degradation of bisphenol A exhibits a volcano-type dependence on annealing temperature, and is maximized for samples treated at 600 °C. The performance of the hydrogenated samples is generally much higher than that of samples calcined in air.
(3) Although the synthesis of photocatalysts with certain properties is crucial to maximize catalytic activity, process performance may also affected by several operating and inherent factors including treatment time, catalyst concentration and stability, as well as the water matrix itself. The latter is critical since its complexity, due to the presence of organics and anions, affects adversely degradation kinetics, i.e. BPA in wastewater is degraded five times slower than in pure water.

BPA degradation at low concentrations follows first order kinetics but this shifts towards zeroth order at higher concentrations. Data fitting to a pseudo-first order expression is, however, adequate for simple kinetic modelling purposes.

(4) The photocatalytic degradation of BPA in the presence of hydrogenated catalysts was found to proceed mainly through hydroxylation pathways yielding hydroxylated and oxidized TBPs. Conversely, para-substituted phenolic TBPs were formed in the presence of calcined catalysts, proving that cleavage of isopropylidene group by hydroxyl radical attack is the main degradation pathway.

Acknowledgements

Part of this work was supported by Grant E056 from the Research Committee of the University of Patras (Program C. Caratheodory).

Part of this research has been co-financed by the European Union (European Social Fund ESF) and Greek national funds through the Operational Program 'Education and Lifelong Learning' of the National Strategic Reference Framework (NSRF)—Research Funding Program: Thales. Investing in knowledge society through the European Social Fund (PhotoFuelCell project).

References

[1] O. Carp, C.L. Huisman, A. Reller, Prog. Solid State Chem. 32 (2004) 33–177.
[2] X. Chen, S.S. Mao, Chem. Rev. 107 (2007) 2891–2959.
[3] K. Nakata, A. Fujishima, J. Photochem. Photobiol. C 13 (2012) 169–189.
[4] X. Chen, C. Burda, J. Am. Chem. Soc. 130 (2008) 5018–5019.
[5] M.R. Hoffmann, S.T. Martin, W. Choi, D.W. Bahnemann, Chem. Rev. 95 (1995) 69–96.
[6] X. Chen, L. Liu, P.Y. Yu, S.S. Mao, Science 331 (2011) 746–750.
[7] G.M. Wang, H.Y. Wang, Y.C. Ling, Y.C. Tang, X.Y. Yang, R.C. Fitzmorris, C.C. Wang, J.Z. Zhang, Y. Li, Nano Lett. 11 (2011) 3026–3033.
[8] G. Li, Z. Zhang, H. Peng, K. Chen, RSC Adv. 3 (2013) 11507–11510.
[9] F. Teng, M. Li, C. Gao, G. Zhang, P. Zhang, Y. Wang, L. Chen, E. Xie, Appl. Catal. B: Environ. 148–149 (2014) 339–343.
[10] W.H. Saputera, G. Mul, M.S. Hamdy, Catal. Today 246 (2015) 60–66.
[11] A.R. Ribeiro, O.C. Nunes, M.F.R. Pereira, A.M.T. Silva, Environ. Int. 75 (2015) 33–51.
[12] J.C. Carlson, M.I. Stefan, J.M. Parnis, C.D. Metcalfe, Water Res. 84 (2015) 350–361.
[13] R.F. Lane, C.D. Adams, S.J. Randtke, R.E. Carter Jr., Water Res. 79 (2015) 68–78.
[14] A. Petala, D. Tsikritzis, M. Kollia, S. Ladas, S. Kennou, D.I. Kondarides, Appl. Surf. Sci. 305 (2014) 281–291.
[15] A. Petala, Z. Frontistis, M. Antonopoulou, I. Konstantinou, D.I. Kondarides, D. Mantzavinos, Water Res. 81 (2015) 157–166.
[16] B. Darsinou, Z. Frontistis, M. Antonopoulou, I. Konstantinou, D. Mantzavinos, Chem. Eng. J. 280 (2015) 623–633.
[17] M.S. Hamdy, P. Nickels, I.H. Abd-Elmaksood, H. Zhou, E.H. El-Mossalamy, A.O. Alyoubi, S. Lynch, A. Nathan, G. Thornton, J. Photochem. Photobiol. A 228 (2012) 1–7.
[18] M.A. Behnajady, M.E. Alamdari, N. Modirshahla, Environ. Prot. Eng. 39 (2013) 33–46.
[19] J. Yu, H. Yu, B. Cheng, M. Zhou, X. Zhao, J. Mol. Catal. A 253 (2006) 112–118.
[20] C.-S. Kim, I.-M. Kwon, B.K. Moon, J.H. Jeong, B.-C. Choi, J.H. Kim, H. Choi, S.S. Yi, D.-H. Yoo, K.-S. Hong, J.-H. Park, H.S. Lee, Mater. Sci. Eng. C 27 (2007) 1343–1346.
[21] J. Wang, G. Zhao, Z. Zhang, X. Zhang, G. Zhang, T. Ma, Y. Jiang, P. Zhang, Y. Li, Dyes Pigm. 75 (2007) 335–343.
[22] T.I. Halkides, D.I. Kondarides, X.E. Verykios, Appl. Catal. B Environ. 41 (2003) 415–426.
[23] K. Lv, Q. Xiang, J. Yuam, Appl. Catal. B Environ. 104 (2011) 275–281.
[24] A. Naldoni, M. Allieta, S. Santangelo, M. Marelli, F. Fabbri, S. Cappelli, C.L. Bianchi, R. Psaro, V. Dal Santo, J. Am. Chem. Soc. 134 (2012) 7600–7603.
[25] Z. Wang, C.Y. Yang, T.Q. Lin, H. Yin, P. Chen, D.Y. Wan, F.F. Xu, F.Q. Huang, J.H. Lin, X.M. Xie, M.H. Jiang, Adv. Funct. Mater. 23 (2013) 5444–5450.
[26] S. Banerjee, S.C. Pillai, P. Falaras, K.E. O'shea, J.A. Byrne, D.D. Dionysiou, J. Phys. Chem. Lett. 5 (2014) 2543–2554.
[27] D. Wang, X. Zhang, P. Sun, S. Lu, L. Wang, C. Wang, Y. Liu, Electrochim. Acta 130 (2014) 290–295.
[28] N. Liu, C. Schneider, D. Freitag, U. Venkatesan, V.R.R. Marthala, M. Hartmann, B. Winter, E. Spiecker, A. Osvet, E.M. Zolnhofer, K. Meyer, T. Nakajima, X. Zhou, P. Schmuki, Angew. Chem. Int. Ed. 53 (2014) 14201–14205.
[29] X. Chen, L. Liu, F. Huang, Chem. Soc. Rev. 44 (2015) 1861–1885.
[30] M.N. Ghazzal, N. Chaoui, M. Genet, E.M. Gaigneaux, D. Robert, Thin Solid Films 520 (2011) 1147–1154.
[31] X. Feng, R. Hock, E. Mankel, D. Lingenfelser, B. Völker, T. Mayer, W. Jaegermann, J. Phys. Chem. C 114 (2010) 20049–20054.
[32] K. Benyamin, Solid State Ionics 73 (1994) 303–308.
[33] M.S. Mattsson, G.A. Niklasson, C.G. Granqvist, J. Appl. Phys. 81 (1997) 2167–2172.
[34] A.G. Thomas, W.R. Flavell, A.K. Mallick, A.R. Kumarasinghe, D. Tsoutsou, N. Khan, C. Chatwin, S. Rayner, G.C. Smith, R.L. Stockbauer, S. Warren, T.K. Johal, S. Patel, D. Holland, A. Taleb, F. Wiame, Phys. Rev. B 75 (2007) (Art. No 035105).
[35] L.-B. Mo, Y. Bai, Q.Y. Xiang, Q. Li, J.O. Wang, K. Ibrahim, J.-L. Cao, Appl. Phys. Lett. 105 (2014) (Art. No 202114).
[36] X. Chen, L. Liu, Z. Liu, M. Marcus, W.C. Wang, N.A. Oyler, M.E. Grass, B. Mao, P. Glans, P.Y. Yu, J. Guo, S.S. Mao, Scientific Reports 3 (2013) (Art. No 1510).
[37] D. Beydoun, R. Amal, G. Low, S. McEvoy, J. Nanopart. Res. 1 (1999) 439–458.
[38] X. Pan, M.-Q. Yang, X. Fu, N. Zhang, Y.-J. Xu, Nanoscale 5 (2013) 3601–3614.
[39] F. Amano, M. Nakata, Appl. Catal. B: Environ. 158–159 (2014) 202–208.
[40] X. Meng, S. Ouyang, T. Kako, P. Li, Q. Yu, T. Wang, J. Ye, Chem. Commun. 50 (2014) 11517–11519.
[41] D. Dimitrakopoulou, I. Rethemiotaki, Z. Frontistis, N.P. Xekoukoulotakis, D. Venieri, D. Mantzavinos, J. Environ. Manage. 98 (2012) 168–174.
[42] J.M. Herrmann, Appl. Catal. B: Environ. 99 (2010) 461–468.
[43] S.P. Azerrad, S. Gur-Reznik, L. Heller-Grossman, C.G. Dosoretz, Water Res. 62 (2014) 107–116.
[44] L.A. Tercero Espinoza, E. ter Haseborg, M. Weber, E. Karle, R. Peschke, F.H. Frimmel, Water Res. 45 (2011) 1039–1048.
[45] L.A. Tercero Espinoza, M. Neamtu, F.H. Frimmel, Water Res. 41 (2007) 4479–4487.
[46] O. Augusto, M.G. Bonini, A.M. Amanso, E. Linares, C.C. Santos, S. Lopes de Menezes, Free Radic. Biol. Med. 32 (2002) 841–859.
[47] M. Antonopoulou, C.G. Skoutelis, C. Daikopoulos, Y. Deligiannakis, I.K. Konstantinou, J. Environ. Chem. Eng. 3 (2015) 3005–3014.
[48] W. Wang, C.-H. Lu, Y.-R. Ni, J.-B. Song, M.-X. Su, Z.-Z. Xu, Catal. Commun. 22 (2012) 19–23.
[49] M.K. Nowotny, L.R. Sheppard, T. Bak, J. Nowotny, J. Phys. Chem. C 112 (2008) 5275–5300.
[50] F. Amano, M. Nakata, K. Asami, A. Yamakata, Chem. Phys. Lett. 579 (2013) 111–113.
[51] S. Sato, Hyomen 28 (1990) 427–437.
[52] J. Tian, Y. Leng, Z. Zhao, Y. Xia, Y. Sang, P. Hao, J. Zhan, M. Li, H. Liu, Nano Energy 11 (2015) 419–427.
[53] S. Li, J. Qiu, M. Ling, F. Peng, B. Wood, S. Zhang, ACS Appl. Mater. Interfaces 5 (2013) 11129–11135.
[54] M. Deborde, S. Rabouan, P. Mazellier, J.-P. Duguet, B. Legube, Water Res. 42 (2008) 4299–4308.
[55] A.O. Kondrakov, A.N. Ignatev, F.H. Frimmel, S. Brase, H. Horn, A.I. Revelsky, Appl. Catal. B: Environ. 160–161 (2014) 106–114.
[56] M. Antonopoulou, A. Giannakas, Y. Deligiannakis, I. Konstantinou, Chem. Eng. J. 231 (2013) 314–325.
[57] A. Kunai, S. Hata, S. Ita, K. Sasaki, J. Am. Chem. Soc. 108 (1986) 6012–6016.
[58] D.P. Subagio, M. Srinivasan, M. Lim, T.T. Lim, Appl. Catal. B Environ. 95 (2010) 414–422.
[59] E. Diez-Mato, F.C. Cortezón-Tamarit, S. Bogialli, D. Garcia-Fresnadillo, M.D. Marazuela, Appl. Catal. B Environ. 160–161 (2014) 445–455.
[60] L.-B. Xiong, J.-L. Li, B. Yang, Y. Yu, J. Nanomater. 2012 (2012) 1–13.